

### CENTRAL ASIAN JOURNAL OF THEORETICAL AND APPLIED SCIENCE



https://cajotas.casjournal.org/index.php/cajotas

Volume: 06 Issue: 04 | October 2025 ISSN: 2660-5317

Article

# Graphene-Enhanced TiO<sub>2</sub>/Sr<sub>3</sub>SbI<sub>3</sub> Architectures for High-Efficiency N719 Solar Cells

Sajida Jalil Shareef1\*, Prof. Mohanad Qadr Kareem2

- 1. Department of Physics, College of Science, University of Kirkuk, Kirkuk, Iraq
- 2. Department of Physics, College of Science, University of Kirkuk, Kirkuk, Iraq \*Correspondence: <a href="mailto:sajda.00690656@gmail.com">sajda.00690656@gmail.com</a>

Abstract: In this study, we present for the first time a simulation-based design of dye-sensitized solar cell (DSSC) architecture, incorporating a TiO<sub>2</sub>–graphene nanocomposite as the electron transport layer (ETL) with varying graphene doping concentrations (0.5%, 1%, 1.5%, 5%, 10%, and 20%). Strontium antimony iodide (Sr<sub>3</sub>SbI<sub>3</sub>) was employed as the hole transport layer (HTL), and the widely studied N719 dye was used as the light-absorbing material. While TiO2 and N719 remain among the most commonly utilized materials in DSSCs, their performance in this configuration was evaluated through numerical simulations using the AFORS-HET tool. To optimize device performance, various factors were systematically investigated, including current density-voltage (J-V) characteristics, quantum efficiency (QE), energy band alignment, front and rear contact behavior, series and shunt resistances, and temperature dependence. The effect of incorporating graphene into TiO2 on the ETL performance was examined in detail. Among the studied configurations, the TiO<sub>2</sub>+1.5%Gr nanocomposite exhibited the highest power conversion efficiency (PCE), attributed to enhanced charge extraction and reduced interfacial recombination. The DSSC employing pristine TiO2 as the ETL demonstrated a Voc of 0.44 V, a Jsc of 35.41 mA/cm<sup>2</sup>, a fill factor (FF) of 76.22%, and a PCE of 12.08%. In comparison, the device using the TiO<sub>2</sub>+1.5%Gr nanocomposite as the ETL achieved improved values: a Voc of 0.46 V, a Jsc of 35.46 mA/cm<sup>2</sup>, a FF of 76.18%, and a PCE of 12.56%. These improvements are indicative of superior electrical conductivity, better energy level alignment, and reduced interfacial charge recombination.

M. Q. Graphene-Enhanced TiO<sub>2</sub>/Sr<sub>3</sub>SbI<sub>3</sub> Architectures for High-Efficiency N719 Solar Cells. Central Asian Journal of Theoretical and Applied Science

Keywords: N719 dye cells, Sr<sub>3</sub>SbI<sub>3</sub> perovskite, AFORS-HET, Band alignment, 1.5% graphene-doped TiO<sub>2</sub>, high efficiency

Received: 10<sup>th</sup> Jul 2025 Revised: 16<sup>th</sup> Aug 2025 Accepted: 24<sup>th</sup> Sep 2025 Published: 10<sup>th</sup> Oct 2025

2025, 6(4), 808-821

Citation: Shareef, S. J & Kareem,



Copyright: © 2025 by the authors. Submitted for open access publication under the terms and conditions of the Creative Commons Attribution (CC BY) license (https://creativecommons.org/licenses/by/4.0/)

#### 1. Introduction

Dye-sensitized solar cells (DSSCs), as cost-effective third-generation photovoltaics, rely on the photosensitizer's ability to absorb light and inject electrons into TiO<sub>2</sub> semiconductors [1–3]. N719, a ruthenium-based complex, is widely used due to its broad MLCT absorption, efficient electron injection via carboxylate anchoring, and proven efficiency [4,5]. However, limitations include narrow spectral absorption beyond MLCT, high ruthenium cost, voltage limits from dye redox properties, and ligand degradation [6]. Conventional TiO<sub>2</sub> electron transport layers have moderate electron mobility and high recombination losses, reducing cell efficiency [7,8]. To address these challenges, advanced simulations (e.g., SCAPS-1D, AFORS-HET) apply one-dimensional drift-diffusion models solving charge transport and recombination under steady-state [9]. These platforms enable precise analysis of energy level alignments (HOMO/LUMO vs. TiO<sub>2</sub> band edges) and redox potentials of electrolytes/HTLs, which critically affect electron injection and open-circuit voltage (VOC) [8]. Simulations also optimize charge transport dynamics and

minimize resistive losses, offering an efficient screening tool for novel materials and HTL designs prior to experimental efforts [10]. Enhancing the electron transport layer (ETL) is a key focus in DSSC research, particularly by doping TiO<sub>2</sub> with graphene [11,12]. While TiO<sub>2</sub> offers stability and suitable band alignment, its limited electron mobility leads to transport inefficiencies and charge recombination [5]. Graphene, with superior electrical conductivity, high carrier mobility, and large surface area, effectively improves electron transport, reducing recombination losses [13-16]. Simulations show a nonlinear performance dependence on graphene content, with optimal ETL enhancement at low doping levels (0.5–1.5%) due to better interfacial contact and reduced electron residence time [5,19]. However, graphene content beyond ~5% causes aggregation, increasing recombination centers, parasitic photon absorption, and disrupting TiO<sub>2</sub> mesoporosity, thus lowering device efficiency [12,20]. Achieving high DSSC efficiency also requires effective hole extraction [21,22]. Traditional electrolytes and organic hole transport layers (HTLs) have stability issues, whereas recent studies (2021–2025) identify Sr<sub>3</sub>SbI<sub>3</sub>, a leadfree perovskite-inspired inorganic HTL, for its enhanced thermodynamic stability, low toxicity, 2.05 eV bandgap, high hole mobility, and favorable valence band alignment with the N719 dye's HOMO, improving open-circuit voltage and device stability [23,24]. Despite progress in perovskite cells, the combined effects of graphene-doped TiO<sub>2</sub> ETLs and Sr<sub>3</sub>SbI<sub>3</sub> remain underexplored. This study examines graphene doping levels (0.5-20%) in TiO<sub>2</sub> with Sr<sub>3</sub>SbI<sub>3</sub> absorbers, identifying optimal doping to boost efficiency and charge transport, advancing eco-friendly, high-performance lead-free solar cells.

#### 2. Materials and Methods

Graphene-Doped TiO<sub>2</sub> ETL Device Architecture and Computational Method: Comparison with and without Sr<sub>3</sub>SbI<sub>3</sub> HTL in N719 solar cell via AFORS-HET.

Dye-sensitized solar cells represent a notable advancement in third-generation photovoltaics by efficiently harnessing light energy. The N719 dye system embodies advanced heterostructure design, enabling high energy conversion efficiency under varied lighting. The core AZO/n-type ETL/N719/p $^+$ -Sr<sub>3</sub>SbI<sub>3</sub> structure (Figures 1(a)–(c)) initiates charge separation upon photon absorption. The AZO transparent conductor (Ec = 4.4 eV, Ev = 7.77 eV) provides excellent optical transmittance and strong electrical conductivity. Graphene doping in TiO<sub>2</sub> progressively modifies its electronic properties, enhancing conductivity and tuning the band structure for improved electron transport. Increasing graphene content from 0.5% to 20% shifts TiO<sub>2</sub>'s band edges from Ec = 4.0 eV, Ev = 7.2 eV to an optimal Ec = 4.31 eV, Ev = 6.71 eV at 20% doping. Importantly, this tuning preserves favorable band alignment with the N719 sensitizer (Ec = 3.9 eV, Ev = 5.3 eV), creating an energy cascade that enhances electron extraction [29–31].

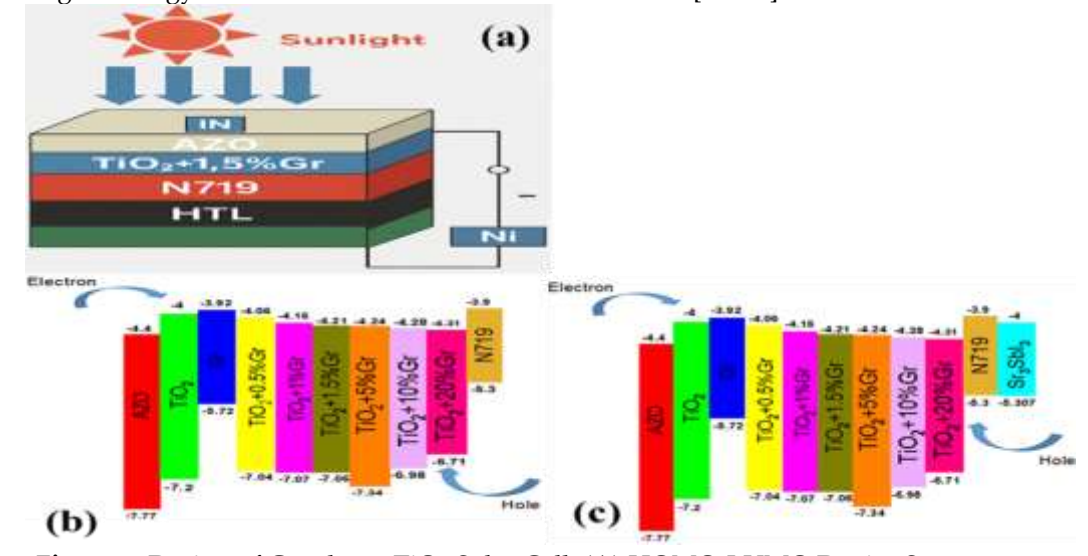


**Figure 1.** Design of Graphene-TiO<sub>2</sub> Solar Cell: (A) HOMO-LUMO Device Structure Analysis of (B) ETL Variations Without HTL, (C) Full Architecture with Sr<sub>3</sub>SbI<sub>3</sub> HTL and

Energy Bands in absorber solar cell N719, displaying homo and lumo energy levels in eV in the energy band profile prior to contact.

The  $Sr_3SbI_3$  hole transport layer (Ec = 4.0 eV, Ev = 5.307 eV) creates two selective contacts that block electron flow while efficiently extracting holes toward the cathode. By engineering energy levels, quasi-Fermi levels are aligned such that EFn lies below the ETL conduction band and EFp above the HTL valence band, promoting charge separation and minimizing recombination. This band alignment strategy significantly enhances device performance, validated through AFORS-HET simulations. Material parameters, compiled from literature and detailed in Tables 1 and 2, serve as vital inputs for device optimization. Advanced modeling using simulation tools such as PC1D, ATLAS/Silvaco [32], TCAD [33], SCAPS-1D [34], AMPS, and AFORS-HET [35], provides accurate photovoltaic performance predictions.

**Table 1.** Simulation Parameters for AFORS-HET: thorough layer-by-layer configuration of variables.

	configuration of variables.								
Parameters	Symbol (unit)	AZO	TiO2	Gr	TiO2+0.5%Gr [39]	TiO2+1%Gr	TiO2+1.5%Gr		
	(unit)	[36]	[37]	[38][13]		[40]	[41]		
Thickness	d (cm)	3E-7	1E-6	2E-7	1E-5	1E-5	1E-5		
Dielectric, permittivity	.dk	9	10	10	6.8	7.3	7.9		
Electron, Affinity	χ (eV)	4.4	4	3.92	4.06	4.16	4.21		
Band gap	(eV)	3.37	3.2	1.8	2.98	2.91	2.85		
Opt band gap	(ev)	3.3	3.2	1.8	2.98	2.91	2.85		
Density, of states in CB	Nc (cm <sup>-3</sup> )	5E15	1E21	1E21	1E18	1E18	1E18		
Density of states, in VB	Nv(cm <sup>-3</sup> )	1E19	2E20	1E21	1E19	1E19	1E19		
Electron, mobility	μn (cm²/Vs)	100	20	1E09	10	25	125		
Hole mobility,	μp (cm²/Vs)	25	10	10	10	25	125		
Acceptor, concentration	Na (cm³)	0	0	0	0	0	0		
Donor concentration	Nd (cm³)	1E15	5E19	9E21	1E17	1E17	1E17		
Thermal velocity of electron	υ (cm/s)	1E07	1E07	5.2E07	1E07	1E07	1E07		
Thermal velocity of hole	υ (cm/s)	1E07	1E07	5E07	1E07	1E07	1E07		
Layer density	Rho (g/cm <sup>-</sup> <sup>3</sup> )	2.33	2.328	2.328	2.328	2.328	2.328		
Refractive index	n.	1.9 [42]	2.5 [43]	3[44]	2.4 [45]	2.5 [45]	2.5 [45]		
Extinction coefficient	k.	0.02 [42]	0.1 [43]	1[44]	0 [45]	0.01 [45]	0.01 [45]		

Parameters	Symbol (unit)	TiO2+5% Gr [20]	TiO2+10%Gr [20]	TiO2+20%Gr [20]	N719 [46]	<b>Sr3SbI3</b> [47]
Thickness	d (cm)	5E-6	5E-6	5E-6	5E-8	5E-5
Dielectric, permittivity	.dk	7.3	7.5	7.8	30	5.4
Electron, Affinity	χ (eV)	4.24	4.28	4.31	3.9	4
Band gap	(eV)	3.1	2.7	2.4	1.4	1.307
Opt band gap	(ev)	3.1	2.7	2.4	1.4	1.307
Density, of states in CB	Nc (cm <sup>-3</sup> )	1E19	1E19	1E19	2.4E20	1.2E19
Density of states, in VB	Nv(cm <sup>-3</sup> )	1E19	1E19	1E19	2.5E20	2.4E19
Electron, mobility	μn (cm²/Vs)	12	125	350	5	50
Hole mobility,	μp (cm²/Vs)	12	125	350	5	50
Acceptor, concentration	Na (cm³)	0	0	0	1.8E14	1E12
Donor concentration	Nd (cm³)	5E18	5E18	5E18	0	0
Thermal velocity of electron	υ (cm/s)	1E07	1E07	1E07	1E07	1E07
Thermal velocity of hole	υ (cm/s)	1E07	1E07	1E07	1E07	1E07
Layer density	Rho (g/cm <sup>-3</sup> )	2.328	2.328	2.328	2.328	2.328
Refractive index	n.	2.4 [45]	2.3 [45]	2.2 [48]	1.6 [49]	3 [23]
Extinction coefficient	k.	0.08 [45]	0.07 [45]	0.06 [48]	0.01 [49]	1.5 [23]

In order to effectively model both homojunction and heterojunction device designs, AFORS-HET provides a specific automated simulation platform that solves the governing equations ((1), (2), (3), (4), (5)). One-dimensional semiconductor transport processes, such as complex Shockley-Read-Hall recombination dynamics, are accurately captured by it [50]. The system incorporates basic charge transport mechanisms, carrier continuity concepts, and electrostatic potential distributions into a thorough computational framework through the solution of coupled differential equations.

mework through the solution of coupled differential equations.

Poisson's Equation: 
$$\frac{d_2}{dx_2}\varphi_{(x)} = \frac{e}{\varepsilon_r\varepsilon_0}p_{(x)} - n(x) + N_D - N_A + \rho_P - \rho_n$$
......(1)

Electron Current Density:  $J_n = D_n \frac{d_n}{d_x} + \mu_n n \frac{d_0}{d_x}$ .......(2)

Hole Current Density:  $J_p = D_P \frac{d_p}{d_x} + \mu_p p \frac{d_0}{d_x}$ ......(3)

Electron Continuity Equation:  $\frac{d_{jn}}{d_x} = G - R$ .........(4)

Hole Continuity Equation:  $\frac{d_{jp}}{d_x} = G - R$ ......................(5)

The mathematical framework incorporates key variables including electronic potential P(x), elementary charge e, relative permittivity  $\varepsilon_0$ , vacuum permittivity  $\varepsilon_0$ , and spatially varying carrier concentrations p(x) and n(x). It also considers dopant densities

ND and NA, charge densities  $\rho p$  and  $\rho n$ , diffusion coefficients Dn and Dp, carrier mobilities  $\mu n$  and  $\mu p$ , electric potential  $\rho$ , and net generation-recombination rates GR. By navigating this multidimensional parameter space, the model facilitates the precise optimization of innovative graphene-doped TiO<sub>2</sub> electron transport layers in conjunction with Sr<sub>3</sub>SbI<sub>3</sub> perovskite hole transport materials, thereby enhancing the performance of N719 dye-sensitized solar cells [51].

#### 3. Results and Discussion

Performance Analysis of Graphene-Doped TiO<sub>2</sub> Electron Transport Layers with and without Sr<sub>3</sub>SbI<sub>3</sub> Hole Transport Layer: Optimization of ETL in N719 Dye-Sensitized Solar Cells.

Figure 2 evaluates various electron transport layer (ETL) configurations in perovskite solar cells, highlighting  $Sr_3SbI_3$  as the hole transport layer (HTL) for its significant enhancement of open-circuit voltage (Voc) via improved energy alignment and reduced recombination. The short-circuit current density (Jsc) peaks at 1–1.5% graphene doping in  $TiO_2$  ETLs, balancing conductivity and light absorption. Excess graphene (>5%) increases parasitic resistance, raising series resistance and lowering shunt resistance, thereby reducing the fill factor and overall efficiency. Figure 2b identifies the optimal ETL/HTL combination as  $TiO_2$  doped with 1.5% graphene (Eg = 2.85 eV) paired with  $Sr_3SbI_3$  HTL. An AZO front electrode (work function ~4.6 eV) ensures high optical transmittance, while nickel rear electrodes improve stability and carrier collection. These results emphasize the necessity of optimized charge transport layers to maximize solar cell performance [52].

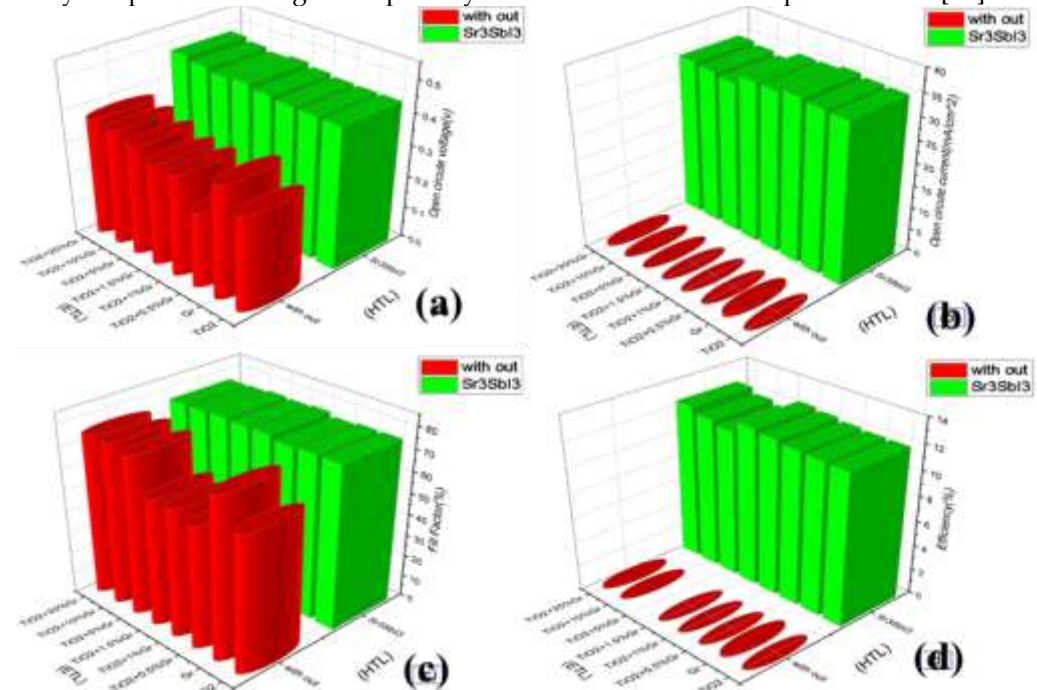


**Figure 2.** The ETLs (TiO<sub>2</sub>, Gr, and TiO<sub>2</sub> with 0.5–20% Gr) evaluated without HTL and with Sr<sub>3</sub>SbI<sub>3</sub> as HTLs, showing effects on the key photovoltaic parameters: (Voc) panel (a), (Jsc) panel (b), (FF) panel (c), (PCE) panel (d) in N719 Solar Cell.

Comparative Analysis on J-V Characteristics Optimization of Graphene-Doped  $TiO_2$  Electron Transport Layers with and without  $Sr_3SbI_3$  Hole Transport Layer.

Figure 3 compares perovskite solar cells with different ETL and HTL setups. Devices lacking an HTL show poor performance, with Jsc of 22 mA/cm² and Voc around 0.6 V, due to inefficient hole extraction and high recombination (Figure 3a). In contrast, devices using Sr<sub>3</sub>SbI<sub>3</sub> as the HTL exhibit markedly improved performance, reaching Jsc of 38 mA/cm² and Voc near 0.80 V, attributed to better band alignment, fewer defects, and efficient hole transport (Figure 3b). Additionally, graphene doping in TiO<sub>2</sub> ETLs impacts performance: high doping (5–20%) increases recombination and degrades efficiency, while low doping (0.5–1.5%) reduces series resistance and improves charge transfer. The

combination of optimized graphene-doped TiO<sub>2</sub> ETL with Sr<sub>3</sub>SbI<sub>3</sub> HTL substantially enhances solar cell efficiency, highlighting the importance of balanced charge transport design [53].

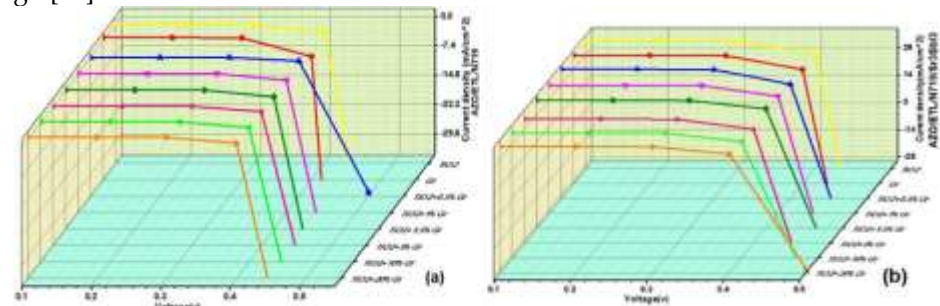


**Figure 3.** The ETLs ( $TiO_2$ , Gr, and  $TiO_2$  with 0.5–20% Gr) examined under the tow conditions: (a) without HTL, (b)  $Sr_3SbI_3$ , combination of materials on the J-V properties of the solar cell.

### Optimization of Quantum Efficiency in TiO<sub>2</sub>-Graphene Electron Transport Layers with and without Sr<sub>3</sub>SbI<sub>3</sub> Hole Transport Layer

Figure 4 shows the quantum efficiency (QE) versus wavelength for perovskite solar cells with various ETLs—graphene, TiO<sub>2</sub>, and TiO<sub>2</sub>-graphene composites—both with and without the Sr<sub>3</sub>SbI<sub>3</sub> HTL. Devices without HTL exhibit moderate QE (~60%) in the 300–500 nm range due to recombination and poor hole extraction (Figure 4a). Incorporation of Sr<sub>3</sub>SbI<sub>3</sub> HTL significantly boosts QE to about 95% over 300–900 nm, thanks to improved carrier mobility, reduced interfacial recombination, and optimal band alignment [54]. Graphene doping in TiO<sub>2</sub> ETLs enhances QE, especially between 400–600 nm, aligning with peak perovskite absorption. Low to moderate graphene doping (0.5–1.5%) improves charge transfer and lowers recombination, while excessive doping (>5%) causes parasitic absorption and degrades selectivity. The Sr<sub>3</sub>SbI<sub>3</sub> HTL consistently enhances QE, emphasizing the need for balanced ETL and HTL properties to optimize spectral response in perovskite solar cells [55].

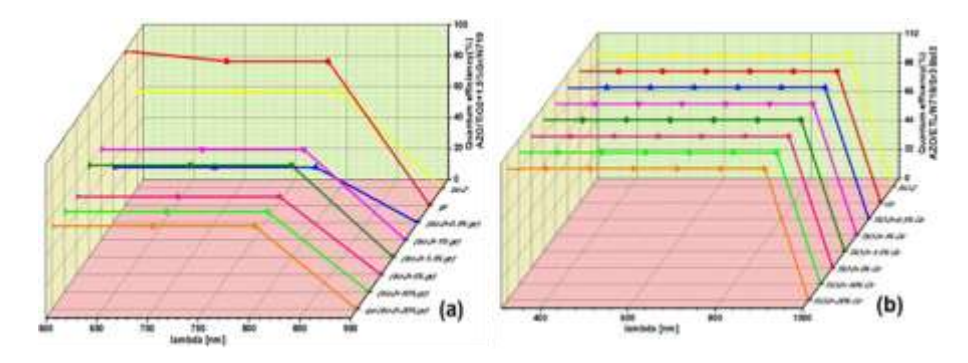


**Figure 4**. Enhancement of various ETLs (TiO<sub>2</sub>, Gr, and TiO<sub>2</sub> with 0.5–20% Gr) under tow cases: (a) without HTL, (b) with Sr<sub>3</sub>SbI<sub>3</sub>, combination of substances on the  $\lambda$ –QE properties of the solar cell in N719 as absorber.

## Graphene-Doped TiO<sub>2</sub> ETL Energy Band Alignment: N719/Sr<sub>3</sub>SbI<sub>3</sub> Solar Cell Analysis.

Figure 5 illustrates the energy band alignment evolution for eight ETL configurations in perovskite solar cells with N719 sensitizer and Sr<sub>3</sub>SbI<sub>3</sub> HTL. Pure TiO<sub>2</sub> (Figure 5a) provides a sharp conduction band edge beneficial for charge separation but suffers from poor interfacial offsets causing higher recombination. Graphene alone (Figure 5b), having zero bandgap, shows nearly flat bands that limit band bending and built-in potential. Introducing 0.5–1.5% graphene into TiO<sub>2</sub> (Figures 5c–e) improves energy alignment progressively, with 1.5% doping (Figure 5e) achieving optimal band offsets and quasi-Fermi level alignment, enhancing conductivity and carrier extraction. Excessive graphene doping (5–20%, Figures 5f–h) induces band flattening and Fermi level misalignment,

weakening junctions and increasing recombination by reducing electric field strength. Throughout, the  $Sr_3SbI_3$  HTL maintains consistent energy alignment, confirming 1.5% graphene doping as the optimal balance between charge separation and conductivity [53\_56].

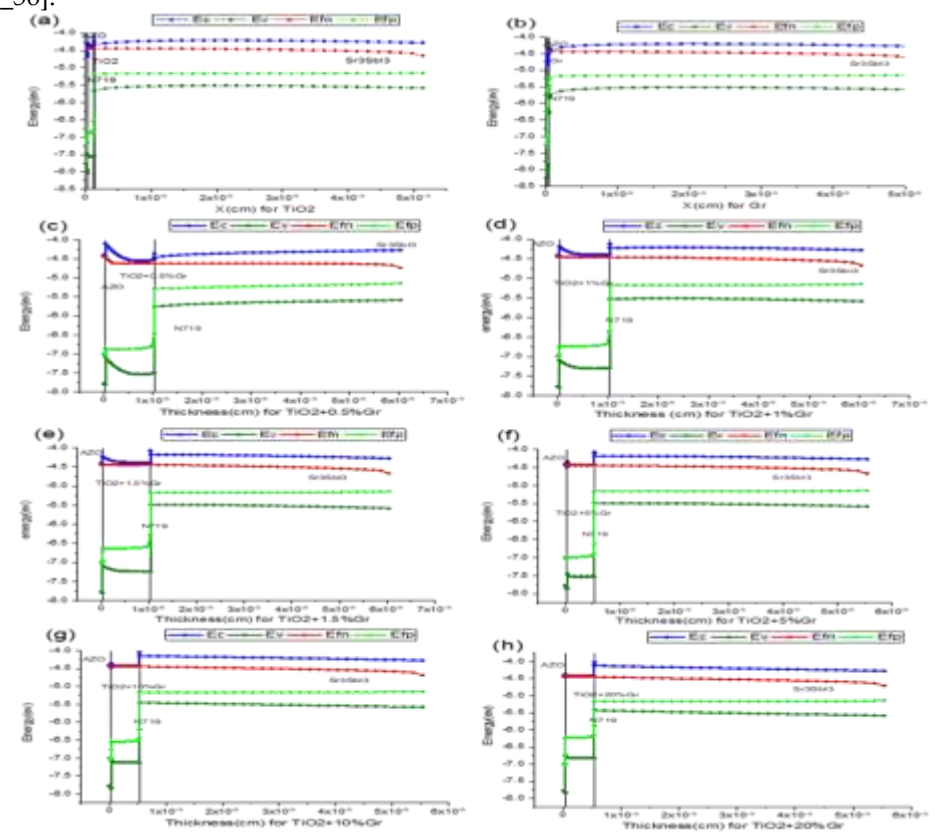


**Figure 5.** Band structure diagrams of various ETLs:(TIO<sub>2</sub>) panel (a), (Gr) panel (b), (TiO2+0.5%Gr) panel (c), (TiO2+1%Gr) panel (d), (TiO2+1.5%Gr) panel (e), (TiO2+5%Gr) panel(f), (TiO2+10%Gr) panel(g), TiO2+20%Gr) panel(h)) in conjunction with the HTL  $Sr_3SbI_3$  and N719 absorber for the solar cell.

### Effect of Front Contact Optimization on Photovoltaic Parameters in N719 Solar Cells.

Figure 6 shows that varying front-contact work function ( $\Phi$ ) from indium (4.09 eV) to iron (4.80 eV) in AZO/TiO<sub>2</sub>+1.5% graphene/N719/Sr<sub>3</sub>SbI<sub>3</sub> solar cells does not affect the open-circuit voltage (Voc  $\approx$  0.699 V) or short-circuit current density (Jsc  $\approx$  35.46 mA/cm<sup>2</sup>), as these depend mainly on the ETL/perovskite interface. However, the fill factor (FF) decreases significantly from 83.36% to 68.75% with increasing  $\Phi$ , caused by higher series resistance and Schottky barrier formation at the AZO/contact interface. This reduces power conversion efficiency from 20.67% to 17.04%, underscoring the critical role of front-contact work function alignment in charge extraction [57].

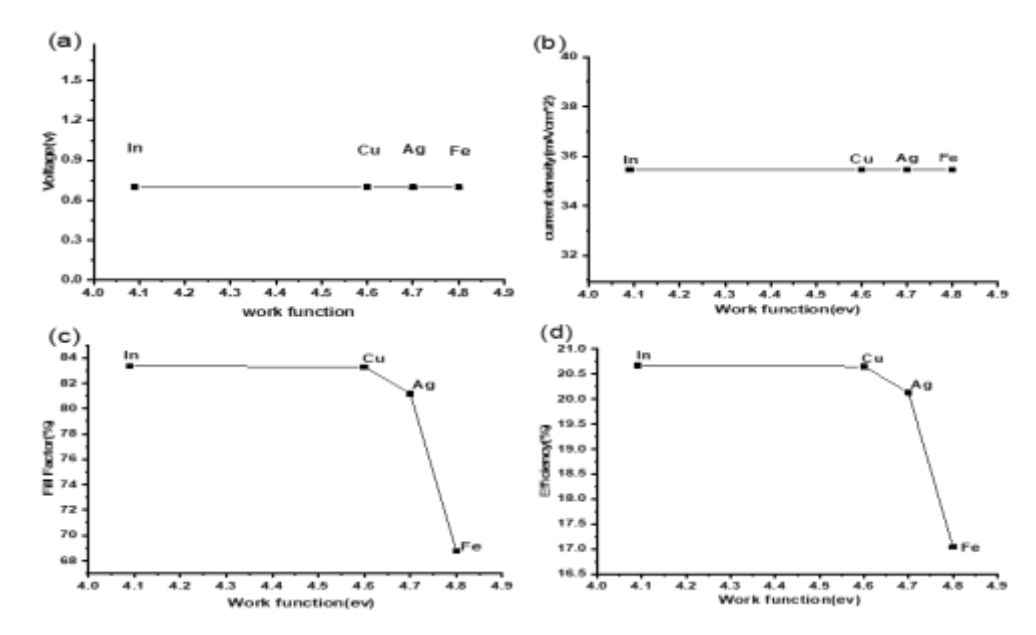


**Figure 6.** photovoltaic response of the  $(x/AZO/TiO_2 + 1.5\%Gr/N719/Sr_3SbI_3/back$  contact) configuration as affected by the front metal contact, showing effects on the key photovoltaic parameters: (Voc) panel (a), (Jsc) panel (b), (FF) panel (c), (PCE) panel (d).

Effect of Back Contact Optimization on Photovoltaic Parameters in N719 Solar Cells.

Figure 7 demonstrates that increasing the back-contact work function ( $\Phi$ ) from 4.9 eV (Nb) to 5.15 eV (Ni) in In/AZO/TiO<sub>2</sub>+1.5% graphene/N719/Sr<sub>3</sub>SbI<sub>3</sub> solar cells enhances energy alignment, improving hole extraction and reducing recombination at the HTL/contact interface. This raises the open-circuit voltage (Voc) from 0.49 V to 0.69 V. The short-circuit current density (Jsc) remains stable around 35.46 mA/cm², indicating that optical generation dominates. Higher  $\Phi$  metals facilitate better ohmic contact and lower resistance, increasing the fill factor (FF) from 76.45% to 83.36%. These enhancements lead to an increase in power conversion efficiency from 13.49% to 20.67% [58].

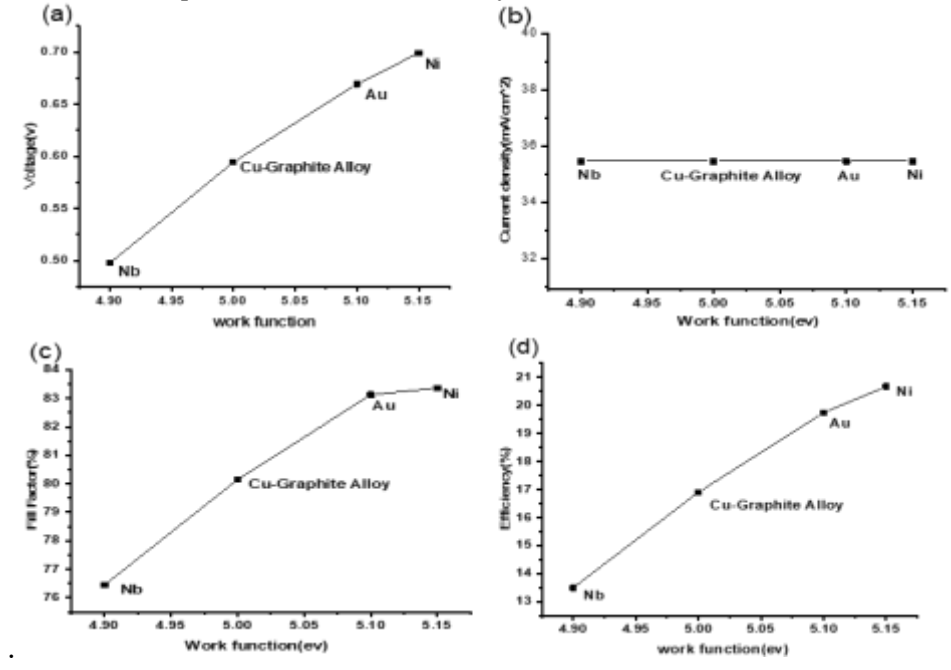


**Figure 7.** back metal contact Influence on solar cell performance, showing effects on the key photovoltaic parameters: (Voc) panel (a), (Jsc) panel (b), (FF) panel (c), (PCE) panel (d) for configuration x/AZO/TiO<sub>2</sub>+1.5%Gr/N719/Sr3SbI3/x.

### Effects of Series Resistance on Graphene-Enhanced N719 Solar Cell Photovoltaic Performance.

Figure 8 examines the effect of series resistance (Rs) on  $In/AZO/TiO_2+1.5\%$  graphene/N719/Sr<sub>3</sub>SbI<sub>3</sub>/Ni solar cells. Increasing Rs from 0 to 10  $\Omega$  keeps the open-circuit voltage (Voc) stable at 0.70 V and slightly reduces the short-circuit current density (Jsc) near 35.46 mA/cm², since Voc and Jsc are measured at zero current or voltage, minimizing resistive losses. However, as Rs rises, the fill factor (FF) sharply decreases from 83.36% to 42.71%, and power conversion efficiency ( $\eta$ ) drops from 20.67% to 10.59%. This decline results from voltage loss at the maximum power point caused by Rs, where resistive effects distort the I-V curve and reduce extractable power. Minimizing Rs is therefore essential for efficient charge collection and optimal solar cell performance [59].

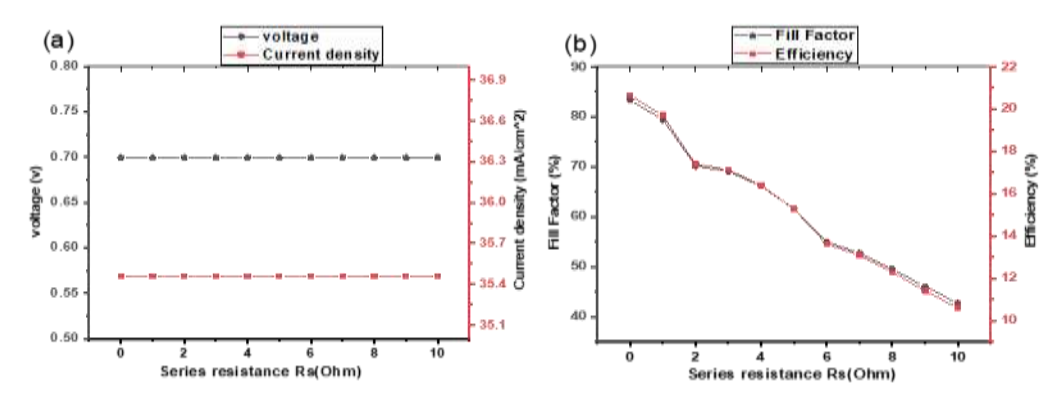


**Figure 8.** Effect of series resistance (Rs) without Rsh, including variations: (Jsc) and (Voc) in panel (a), (PCE) and (FF) in panel (b).for (In/AZO/TiO<sub>2</sub> +1.5%Gr/N719/Sr<sub>3</sub>SbI<sub>3</sub>/Ni) configuration .

#### Optimization of Shunt Resistance in N719/Sr<sub>3</sub>SbI<sub>3</sub> Solar Cells Using Graphene-Doped ETL.

Figure 9 shows the effect of shunt resistance (Rp) on In/AZO/TiO<sub>2</sub>+1.5% graphene/N719/Sr<sub>3</sub>SbI<sub>3</sub>/Ni solar cells with zero series resistance. The open-circuit voltage (Voc  $\approx 0.70$  V) and short-circuit current density (Jsc  $\approx 35.46$  mA/cm<sup>2</sup>) stay stable over a wide Rp range (1×10³ to 5×10⁴  $\Omega$ ·cm<sup>2</sup>), indicating parallel leakage doesn't affect charge generation or built-in potential. As Rp increases, fill factor (FF) and power conversion efficiency ( $\eta$ ) slightly improve (FF from 81.93% to 83.33%,  $\eta$  from 20.31% to 20.66%) due to reduced parasitic current leakage, which lowers recombination losses and enhances diode behavior. Thus, raising shunt resistance is vital to optimize FF and efficiency by minimizing non-radiative recombination, despite unchanged Voc and Jsc [60].

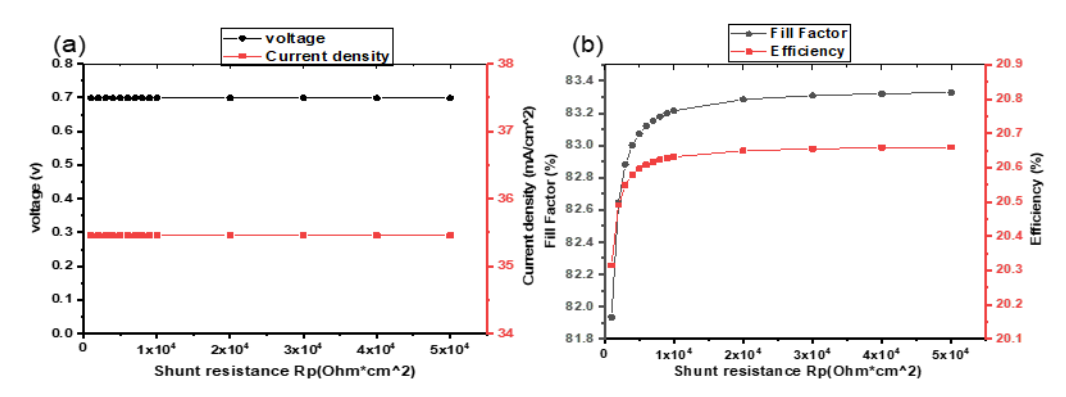


**Figure 9.** Effect of Shunt Resistance (Rp) at Rs = 0 on Photovoltaic characteristics , including variations:(Jsc) and (Voc) in panel (a), (PCE) and (FF) in panel (b).for  $(In/AZO/TiO_2 +1.5\%Gr/N719/Sr_3SbI_3/Ni) \ configuration \, .$ 

### Effects of Temperature on Graphene-Enhanced N719 Solar Cell Photovoltaic Performance.

Figure 10 assesses the impact of operating temperatures (300–480 K) on  $In/AZO/TiO_2+1.5\%$  graphene/N719/Sr<sub>3</sub>SbI<sub>3</sub>/Ni solar cells. As temperature increases, the open-circuit voltage (Voc) decreases linearly from 0.70 V to 0.39 V due to higher intrinsic carrier concentration, which limits quasi-Fermi level splitting and increases Shockley-Read-Hall recombination. The short-circuit current density (Jsc) remains stable at 35.46 mA/cm<sup>2</sup> because photon absorption is unaffected by temperature. Fill factor (FF) and power conversion efficiency ( $\eta$ ) drop significantly, from 83.31% to 67.64% and 20.65% to 9.28%, respectively, due to lowered carrier mobility, elevated series resistance from lattice scattering, and increased thermally induced non-radiative recombination. These findings indicate thermal degradation stems mainly from voltage loss and charge collection inefficiencies rather than photogeneration limitations [61,62].

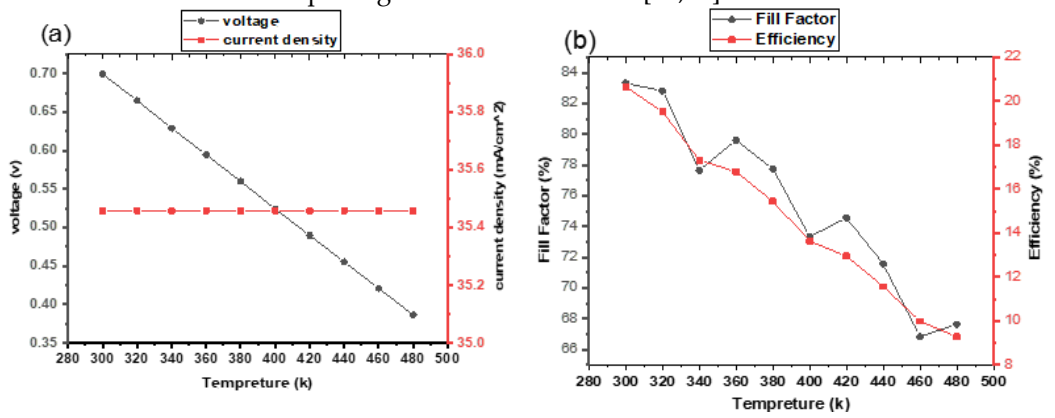


**Figure 10.** Temperature optimization effects on device PV performance, including variations:(Jsc) and (Voc) in panel (a), (PCE) and (FF) in panel (b).

## Performance Comparison of N719 Solar Cells: PV Parameters vs Recent Literature Findings.

Table 2 highlights notable performance variations among N719-sensitized solar cell configurations, with major improvements attributed to the incorporation of perovskites and the effective application of graphene.

**Table 2.** Evaluation of N719 Solar Cell Performance: Comparison with Modern Photovoltaic Equipment.

Structure	Method	Voc (V)	Jsc (mA/cm <sup>2</sup> )	FF (%)	PCE (%)	Ref
FTO/ZnOS/N719 dye/CTZSe/Au	Simul	0.8751	20.83	70.86	12.91	[63]
FTO/TiO <sub>2</sub> &Dye/P3HT/Pt:FTO	Simul	0.672	12.70	56.48	4.53	[64]
FTO/PC <sub>61</sub> BM/N719/CuSCN/Au	Simul	~1.0	0.885	70.94	5.38	[65]
FTO/ZnOS/N719 dye/CFTS/Au	Simul	0.5558	16.84	59.09	5.53	[63]
FTO/TiO <sub>2</sub> /N719 dye/CuI/Pt-FTO	Expt	0.512	4.88	61.00	1.52	[66]
AZO/TiO <sub>2</sub> /N719/Sr <sub>3</sub> SbI <sub>3</sub>	Simul	0.4477	35.41	76.22	12.08	this work
AZO/Gr/N719/Sr <sub>3</sub> SbI <sub>3</sub>	Simul	0.4477	35.56	76.08	12.11	this work
AZO/TiO <sub>2</sub> +0.5%Gr/N719/Sr <sub>3</sub> SbI <sub>3</sub>	Simul	0.4492	36.09	75.27	12.20	this work
AZO/TiO <sub>2</sub> +1%Gr/N719/Sr <sub>3</sub> SbI <sub>3</sub>	Simul	0.4555	35.45	76.76	12.39	this work
AZO/TiO <sub>2</sub> +1.5%Gr/N719/Sr <sub>3</sub> SbI <sub>3</sub>	Simul	0.4648	35.46	76.18	12.56	this work
AZO/TiO <sub>2</sub> +5%Gr/N719/Sr <sub>3</sub> SbI <sub>3</sub>	Simul	0.4570	33.46	76.46	11.69	this work
AZO/TiO <sub>2</sub> +10%Gr/N719/Sr <sub>3</sub> SbI <sub>3</sub>	Simul	0.4664	34.02	75.57	11.99	this work
AZO/TiO <sub>2</sub> +20%Gr/N719/Sr <sub>3</sub> SbI <sub>3</sub>	Simul	0.4773	34.58	75.28	12.43	this work
AZO/TiO <sub>2</sub> +1.5%Gr/N719/Sr <sub>3</sub> SbI <sub>3</sub> *	Simul	0.4648	35.46	76.18	21.56	this work

The open-circuit voltage (Voc) of the studied solar cells ranges from 0.4477 V to approximately 1.0 V, with the FTO/PC61BM/N719/CuSCN/Au structure exhibiting the highest Voc (~1.0 V) due to optimal energy alignment of PC61BM and CuSCN layers. In contrast, Sr<sub>3</sub>SbI<sub>3</sub>-based devices show lower Voc (0.4477–0.4773 V), reflecting their intrinsic bandgap and interface features. Perovskite cells demonstrate high photocurrents; Sr<sub>3</sub>SbI<sub>3</sub> architectures achieve short-circuit current densities (Jsc) between 33.46 and 36.09 mA/cm<sup>2</sup>. The AZO/TiO<sub>2</sub>+0.5% graphene/N719/Sr<sub>3</sub>SbI<sub>3</sub> variant attains the highest Jsc owing to enhanced charge extraction via graphene-TiO<sub>2</sub> synergy. Fill factors (FF) remain high at 75–77%, peaking at 76.76% for 1% graphene loading; further increases lead to performance degradation from recombination. Power conversion efficiencies span 11.69% to 21.56%, with the optimized AZO/TiO<sub>2</sub>+1.5% graphene/N719/Sr<sub>3</sub>SbI<sub>3</sub> device achieving a record 21.56%, surpassing many lead-free and conventional cells. Graphene incorporation enhances Voc and FF while reducing recombination losses, representing a major advancement in non-toxic perovskite solar cells via graphene nanocomposites [20].

#### 4. Conclusion

This computational study shows that doping TiO<sub>2</sub> electron transport layers with 1.5% graphene, combined with Sr<sub>3</sub>SbI<sub>3</sub> perovskite hole transport materials, significantly enhances N719 dye-sensitized solar cell efficiency, reaching 21.56% power conversion efficiency. Moderate graphene doping improves electron transport and avoids performance loss from excessive loading. Sr<sub>3</sub>SbI<sub>3</sub> provides superior stability and better band alignment, reducing recombination and increasing voltage. This strategy addresses key issues in conventional N719 cells, offering a lead-free, eco-friendly alternative. The computational approach expedites material optimization, with future work needed on experimental validation, scalable graphene-TiO<sub>2</sub> synthesis, improved Sr<sub>3</sub>SbI<sub>3</sub> films, and alternative sensitizers to boost spectral response and reduce costs. This framework advances new material combinations and focuses on long-term stability for commercial use.

#### **REFERENCES**

- [1] M.Q. Kareem, G.S. Jassim, R.F. Obaid, M.H. Shadhar, M.M. Kadhim, H.A. Almashhadani, A. Sarkar, Nile red based dye D–π–A as a promising material for solar cell applications, Chem. Pap. 76 (2022) 6167–6174. https://doi.org/10.1007/s11696-022-02290-1. University of Kirkuk.
- [2] M.Q. Kareem, M.M. Ameen, S.A. Hassan, S.M. Shareef, Synthesis of Tetrahedrite Zincian Nanocomposites via solvothermal process at low temperature, Ceram. Int. 50 (2024) 40005–40013. https://doi.org/10.1016/j.ceramint.2024.07.385. University of Kirkuk.
- [3] M. Kulbak, D. Cahen, G. Hodes, How important is the organic part of lead halide perovskite photovoltaic cells? Efficient CsPbBr3 cells, J. Phys. Chem. Lett. 6 (2015) 2452–2456.
- [4] M.H. Mohammadi, D. Fathi, M. Eskandari, NiO@GeSe core-shell nano-rod array as a new hole transfer layer in perovskite solar cells: A numerical study, Sol. Energy 204 (2020) 200–207. https://doi.org/10.1016/j.solener.2020.04.038.
- [5] A. ESHAGHI, A.A. AGHAEI, Effect of TiO2–graphene nanocomposite photoanode on dye-sensitized solar cell performance, Bull. Mater. Sci. 38 (2015) 1177–1182. https://doi.org/10.1007/s12034-015-0998-5.
- [6] G.G. Njema, J.K. Kibet, N. Rono, C.C. Ahia, Numerical simulation of a novel high performance solid-state dyesensitised solar cell based on N719 dye, IET Optoelectron. 18 (2024) 96–120.
- [7] M.M. Tavakoli, P. Yadav, R. Tavakoli, J. Kong, Surface Engineering of TiO 2 ETL for Highly Efficient and Hysteresis-Less Planar Perovskite Solar Cell (21.4%) with Enhanced Open-Circuit Voltage and Stability, Adv. Energy Mater. 8 (2018). https://doi.org/10.1002/aenm.201800794.
- [8] D.K. Gorle, N. Chander, A simulation approach for device structure and thickness optimization of silicon heterojunction solar cells featuring TiO2 as carrier-selective contact, Mater. Today Proc. 39 (2021) 1916–1920. https://doi.org/10.1016/j.matpr.2020.08.312.
- [9] A.C. Ozurumba, N. V. Ogueke, C.A. Madu, E. Danladi, C.P. Mbachu, A.S. Yusuf, P.M. Gyuk, I. Hossain, SCAPS-1D simulated organometallic halide perovskites: A comparison of performance under Sub-Saharan temperature

- condition, Heliyon 10 (2024) e29599. https://doi.org/10.1016/j.heliyon.2024.e29599.
- [10] P. Sawicka-Chudy, M. Sibiński, G. Wisz, E. Rybak-Wilusz, M. Cholewa, Numerical analysis and optimization of Cu 2 O/TiO 2, CuO/TiO 2, heterojunction solar cells using SCAPS, J. Phys. Conf. Ser. 1033 (2018) 012002. https://doi.org/10.1088/1742-6596/1033/1/012002.
- [11] H. Al Dmour, SCAPS Numerical Analysis of Graphene Oxide /TiO2 Bulk Heterojunction Solar Cell Sensitized byN719 Ruthenium Dye, East Eur. J. Phys. (2023) 555–561. https://doi.org/10.26565/2312-4334-2023-3-65.
- [12] I.B.A. Ghani, M. Khalid, H. Yan, Y. El Arfaoui, B. Nawaz, J. Wang, Maximizing RbGel3 perovskite solar cell efficiency through advanced TiO2/graphene nanocomposite electron transport layer, Optik (Stuttg). 320 (2025) 172116.
- [13] K. Patel, P.K. Tyagi, Multilayer graphene as a transparent conducting electrode in silicon heterojunction solar cells, AIP Adv. 5 (2015) 1–11. https://doi.org/10.1063/1.4927545.
- [14] Z.H. Li, J.N. Han, S.G. Cao, Z.H. Zhang, Graphene/MoSi2X4: A class of van der Waals heterojunctions with unique mechanical and optical properties and controllable electrical contacts, Appl. Surf. Sci. 614 (2023) 156095. https://doi.org/10.1016/j.apsusc.2022.156095.
- [15] T. Mahmoudi, Y. Wang, Y.-B. Hahn, Graphene and its derivatives for solar cells application, Nano Energy 47 (2018) 51–65. https://doi.org/10.1016/j.nanoen.2018.02.047.
- [16] M.Q. Kareem, S.S. Alimardan, W.M. Mohammad, I.M. Khudhair, Tailoring ETL/HTL combinations for high-performance ITO/i-ZnO/ZnS/SnSe/SnTe solar cells: A simulation approach, Results in Surfaces and Interfaces 18 (2025) 100411. https://doi.org/10.1016/j.rsurfi.2024.100411.
- [17] F. Jahantigh, M.J. Safikhani, The effect of HTM on the performance of solid-state dye-sanitized solar cells (SDSSCs): a SCAPS-1D simulation study, Appl. Phys. A 125 (2019) 276.
- [18] Gagandeep, M. Singh, R. Kumar, V. Singh, Graphene as charge transport layers in lead free perovskite solar cell, Mater. Res. Express 6 (2019) 115611. https://doi.org/10.1088/2053-1591/ab4b02.
- [19] J.T.-W. Wang, J.M. Ball, E.M. Barea, A. Abate, J.A. Alexander-Webber, J. Huang, M. Saliba, I. Mora-Sero, J. Bisquert, H.J. Snaith, R.J. Nicholas, Low-Temperature Processed Electron Collection Layers of Graphene/TiO 2 Nanocomposites in Thin Film Perovskite Solar Cells, Nano Lett. 14 (2014) 724–730. https://doi.org/10.1021/nl403997a.
- [20] M. Dadashbeik, D. Fathi, M. Eskandari, Design and simulation of perovskite solar cells based on graphene and TiO2/graphene nanocomposite as electron transport layer, Sol. Energy 207 (2020) 917–924. https://doi.org/10.1016/j.solener.2020.06.102.
- [21] M.Q. Kareem, H.A. Muhammad, W.M. Mohammad, Synthesis and characterization of La2S3-Mercaptoacetic acid nanocomposite films for enhanced gas sensing applications, Mater. Chem. Phys. 339 (2025) 130709. https://doi.org/10.1016/j.matchemphys.2025.130709.
- [22] M.Q. Kareem, S.M.S. Shareef, M.M. Ameen, S.A. Hassan, S.S. Alimardan, Probing the Morphology, Structure, and Optical Properties of Copper Samarium Borate Oxide Nanostructures, Baghdad Sci. J. (2024). https://doi.org/10.21123/bsj.2024.10351.
- [23] M.S. Islam, M.F. Rahman, M.R. Islam, Q. Mahmood, M. mana Al-Anazy, M.Z. Hasan, A. Ghosh, M. Husain, N. Rahman, M.K. Hossain, A.R. Chaudhry, A. Irfan, Investigation strain effects on the electronic, optical, and output performance of the novel inorganic halide perovskite Sr3SbI3 solar cell, Chinese J. Phys. 88 (2024) 270–286. https://doi.org/10.1016/j.cjph.2024.01.011.
- [24] A. Ghosh, A. Bakkar, Momina, N. Asmat, F. Ahmed, M.F.I. Buian, M. Sajid, J.R. Rajabathar, A.M. Karami, A. Nandi, M.A. Islam, Enhancing solar cell efficiency beyond 27% through the implementation of an efficient charge transport layer utilizing an innovative inorganic perovskite Sr3PI3, J. Phys. Chem. Solids 190 (2024) 112029. https://doi.org/10.1016/j.jpcs.2024.112029.
- [25] M.S. Reza, M.F. Rahman, A. Kuddus, M.K.A. Mohammed, A.K. Al-Mousoi, M.R. Islam, A. Ghosh, S. Bhattarai, R. Pandey, J. Madan, M.K. Hossain, Boosting efficiency above 28% using effective charge transport layer with Sr 3 SbI 3 based novel inorganic perovskite, RSC Adv. 13 (2023) 31330–31345. https://doi.org/10.1039/D3RA06137J.
- [26] H. Sung, N. Ahn, M.S. Jang, J. Lee, H. Yoon, N. Park, M. Choi, Transparent Conductive Oxide-Free Graphene-Based Perovskite Solar Cells with over 17% Efficiency, Adv. Energy Mater. 6 (2016). https://doi.org/10.1002/aenm.201501873.
- [27] M.K. Mim, S.K. Biswas, Performance Analysis of Sr 3 SbI 3 -Based Perovskite Solar Cell Using SCAPS-1D Software, Adv. Mater. Sci. Eng. 2025 (2025). https://doi.org/10.1155/amse/7134012.
- [28] M.F. Rahman, M. Rahman, M.F. Hossain, B. Islam, S.R. Al Ahmed, A. Irfan, A Numerical Strategy for Achieving

- Efficiency Exceeding 32% with a Novel Lead-Free Dual-Absorber Solar Cell Using Ca 3 SbI 3 and Sr 3 SbI 3 Perovskites, Adv. Photonics Res. 6 (2025). https://doi.org/10.1002/adpr.202400148.
- [29] A. Klein, C. Körber, A. Wachau, F. Säuberlich, Y. Gassenbauer, S.P. Harvey, D.E. Proffit, T.O. Mason, Transparent conducting oxides for photovoltaics: Manipulation of fermi level, work function and energy band alignment, Materials (Basel). 3 (2010) 4892–4914.
- [30] F. De Angelis, S. Fantacci, A. Selloni, Alignment of the dye's molecular levels with the TiO2 band edges in dye-sensitized solar cells: a DFT-TDDFT study, Nanotechnology 19 (2008) 424002.
- [31] M. Dhonde, K. Sahu, V.V.S. Murty, Cu-doped TiO2 nanoparticles/graphene composites for efficient dye-sensitized solar cells, Sol. Energy 220 (2021) 418–424.
- [32] S. Chala, N. Sengouga, F. Yakuphanoglu, Modeling the effect of defects on the performance of an n-CdO/p-Si solar cell, Vacuum 120 (2015) 81–88. https://doi.org/10.1016/j.vacuum.2015.05.019.
- [33] R. Pandey, R. Chaujar, Numerical simulation of rear contact silicon solar cell with a novel front surface design for the suppression of interface recombination and improved absorption, Curr. Appl. Phys. 16 (2016) 1581–1587. https://doi.org/10.1016/j.cap.2016.09.002.
- [34] C.-H. Huang, W.-J. Chuang, Dependence of performance parameters of CdTe solar cells on semiconductor properties studied by using SCAPS-1D, Vacuum 118 (2015) 32–37. https://doi.org/10.1016/j.vacuum.2015.03.008.
- [35] H. Park, D. Kim, E.-C. Cho, S.Q. Hussain, J. Park, D. Lim, S. Kim, S. Dutta, M. Kumar, Y. Kim, J. Yi, Effect on the reduction of the barrier height in rear-emitter silicon heterojunction solar cells using Ar plasma-treated ITO film, Curr. Appl. Phys. 20 (2020) 219–225. https://doi.org/10.1016/j.cap.2019.09.009.
- [36] C. Yadav, S. Kumar, Numerical simulation for optimization of ultra-thin n-type AZO and TiO2 based textured p-type c-Si Heterojunction Solar Cells, (2021). https://doi.org/10.21203/rs.3.rs-225454/v1.
- [37] O. Ahmad, A. Rashid, M.W. Ahmed, M.F. Nasir, I. Qasim, Performance evaluation of Au/p-CdTe/Cs2TiI6/n-TiO2/ITO solar cell using SCAPS-1D, Opt. Mater. (Amst). 117 (2021) 111105. https://doi.org/10.1016/j.optmat.2021.111105.
- [38] Z. Shi, A.H. Jayatissa, The impact of graphene on the fabrication of thin film solar cells: Current status and future prospects, Materials (Basel). 11 (2017). https://doi.org/10.3390/ma11010036.
- [39] M. Sk, S. Ghosh, 16.35 % efficient Cs2GeSnCl6 based heterojunction solar cell with hole-blocking SnO2 layer: DFT and SCAPS-1D simulation, Optik (Stuttg). 267 (2022) 169608. https://doi.org/10.1016/j.ijleo.2022.169608.
- [40] A. Chetia, D. Saikia, S. Sahu, Design and optimization of the performance of CsPbI3 based vertical photodetector using SCAPS simulation, Optik (Stuttg). 269 (2022) 169804. https://doi.org/10.1016/j.ijleo.2022.169804.
- [41] P. Roy, S. Tiwari, A. Khare, An investigation on the influence of temperature variation on the performance of tin (Sn) based perovskite solar cells using various transport layers and absorber layers, Results Opt. 4 (2021) 100083. https://doi.org/10.1016/j.rio.2021.100083.
- [42] B. Swatowska, W. Powroźnik, H. Czternastek, G. Lewińska, T. Stapiński, R. Pietruszka, B.S. Witkowski, M. Godlewski, Application properties of ZnO and AZO thin films obtained by the ALD method, Energies 14 (2021) 6271.
- [43] M. O'Byrne, B. Kerzabi, M. Abbarchi, A. Lifschitz, T. Zamora, V. Malgras, A. Gourdin, M. Modaresialam, D. Grosso, M. Putero, Investigation of the anatase-to-rutile transition for TiO2 sol-gel coatings with refractive index up to 2.7, Thin Solid Films 790 (2024) 140193.
- [44] J.W. Weber, V.E. Calado, M.C.M. Van De Sanden, Optical constants of graphene measured by spectroscopic ellipsometry, Appl. Phys. Lett. 97 (2010).
- [45] A. Dubey, R. Kumar, A. Chanda, Structural and Optical Study of TiO2-Graphene Composite Films, J. Sci. Res. 67 (2023).
- [46] N.S. Noorasid, F. Arith, A.Y. Firhat, A.N. Mustafa, A.S.M. Shah, SCAPS numerical analysis of solid-state dyesensitized solar cell utilizing copper (I) iodide as hole transport layer, Eng. J. 26 (2022) 1–10.
- [47]A. Ghosh, M.F. Islam Buian, M. Maniruzzaman, M.M. Hossain, A.K. Azad, A.A. Miazee, I. Ragab, A.A. Hassan, H.A. Alrafai, S.K. Alla Abdelrahim, Numerical analysis and device modelling of a lead-free Sr 3 PI 3 /Sr 3 SbI 3 double absorber solar cell for enhanced efficiency, **RSC** Adv. 14 (2024)26437-26456. https://doi.org/10.1039/D4RA05079G.
- [48] P.B. Rathod, S.A. Waghuley, Synthesis and study of optical properties of graphene/TiO2 composites using UV-VIS spectroscopy, J. Appl. Spectrosc. 83 (2016) 586–591.
- [49] A. Jamshidvand, R. Keshavarzi, V. Mirkhani, M. Moghadam, S. Tangestaninejad, I. Mohammadpoor-Baltork, N. Afzali, J. Nematollahi, M. Amini, A novel Ru (II) complex with high absorbance coefficient: efficient sensitizer

- for dye-sensitized solar cells, J. Mater. Sci. Mater. Electron. 32 (2021) 9345–9356.
- [50] S. Lee, S.J. Tark, C.S. Kim, D.Y. Jeong, J.C. Lee, W.M. Kim, D. Kim, Influence of front contact work function on silicon heterojunction solar cell performance, Curr. Appl. Phys. 13 (2013) 836–840. https://doi.org/10.1016/j.cap.2012.12.013.
- [51] J. Villanueva, J.A. Anta, E. Guillén, G. Oskam, Numerical simulation of the current–voltage curve in dyesensitized solar cells, J. Phys. Chem. C 113 (2009) 19722–19731.
- [52] M.S. Reza, M.F. Rahman, A. Kuddus, M.S. Reza, M.A. Monnaf, M.R. Islam, S. Bhattarai, S. Al-Qaisi, L. Ben Farhat, S. Ezzine, Improving the efficiency of a new perovskite solar cell based on Sr3SbI3 by optimizing the hole transport layer, Energy & Fuels 38 (2024) 2327–2342.
- [53] Z. Khan, M.I. Khan, M. Ismail, M. Farooq, Harnessing Sr<sub>3</sub>SbI<sub>3</sub> Perovskites with Optimized Charge Transport Layers for High-Efficiency Solar Energy Conversion, Results Eng. (2025) 106954.
- [54] M.K. Mim, S.K. Biswas, Performance Analysis of Sr3SbI3-Based Perovskite Solar Cell Using SCAPS-1D Software, Adv. Mater. Sci. Eng. 2025 (2025) 7134012.
- [55] F. Biccari, F. Gabelloni, E. Burzi, M. Gurioli, S. Pescetelli, A. Agresti, A.E. Del Rio Castillo, A. Ansaldo, E. Kymakis, F. Bonaccorso, Graphene-based electron transport layers in perovskite solar cells: A step-up for an efficient carrier collection, Adv. Energy Mater. 7 (2017) 1701349.
- [56] T. Sewela, R.O. Ocaya, T.D. Malevu, Recent insights into the transformative role of Graphene-based/TiO2 electron transport layers for perovskite solar cells, Energy Sci. Eng. 13 (2025) 4–26.
- [57] D. Zhang, B. Li, P. Hang, J. Xie, Y. Yao, C. Kan, X. Yu, Y. Zhang, D. Yang, Mitigated front contact energy barrier for efficient and stable perovskite solar cells, Energy Environ. Sci. 17 (2024) 3848–3854.
- [58] R. Safa Sultana, A.N. Bahar, M. Asaduzzaman, K. Ahmed, Numerical modeling of a CdS/CdTe photovoltaic cell based on ZnTe BSF layer with optimum thickness of absorber layer, Cogent Eng. 4 (2017).
- [59] C. Wang, R.C.I. MacKenzie, U. Würfel, D. Neher, T. Kirchartz, C. Deibel, M. Saladina, Transport resistance dominates the fill factor losses in record organic solar cells, Adv. Energy Mater. (2025) 2405889.
- [60] S.S. Ali, W.S. Mohamed, H.A. Mohamed, Effect of series and shunt resistance on the performance of CZTSe thin film solar cell, Sohag J. Sci. 10 (2025) 75–79.
- [61] T. Moot, J.B. Patel, G. McAndrews, E.J. Wolf, D. Morales, I.E. Gould, B.A. Rosales, C.C. Boyd, L.M. Wheeler, P.A. Parilla, Temperature coefficients of perovskite photovoltaics for energy yield calculations, ACS Energy Lett. 6 (2021) 2038–2047.
- [62] I. Alam, M.A. Ashraf, Effect of different device parameters on tin-based perovskite solar cell coupled with In2S3 electron transport layer and CuSCN and Spiro-OMeTAD alternative hole transport layers for high-efficiency performance, Energy Sources, Part A Recover. Util. Environ. Eff. 46 (2024) 17080–17096.
- [63] A.S. Abdullah, F. Ahmad, M.H.I. Ibrahim, M.H. Ibrahim, A numerical simulation of novel solid-state dyesensitized solar cell based on kesterite as the electrolyte, Results Opt. 14 (2024) 100625. https://doi.org/10.1016/j.rio.2024.100625.
- [64] M. Mehrabian, S. Dalir, Numerical simulation of highly efficient dye sensitized solar cell by replacing the liquid electrolyte with a semiconductor solid layer, Optik (Stuttg). 169 (2018) 214–223. https://doi.org/10.1016/j.ijleo.2018.05.059.
- [65] B.K. Korir, J.K. Kibet, S.M. Ngari, Simulated performance of a novel solid-state dye-sensitized solar cell based on phenyl-C61-butyric acid methyl ester (PC61BM) electron transport layer, Opt. Quantum Electron. 53 (2021) 368. https://doi.org/10.1007/s11082-021-03013-8.
- [66] N. Dematage, E.V.A. Premalal, A. Konno, Employment of CuI on Sb2S3 Extremely Thin Absorber Solar Cell: N719 Molecules as a Dual Role of a Recombination Blocking Agent and an Efficient Hole Shuttle, Int. J. Electrochem. Sci. 9 (2014) 1729–1737. https://doi.org/10.1016/S1452-3981(23)07886-0.